Journal Name

ARTICLE TYPE

Cite this: DOI: 00.0000/xxxxxxxxxx

Interplay between magnetic order and electronic band structure in ultrathin $GdGe_2$ metalloxene films†

Andrey V. Matetskiy,*[a,b] Valeria Milotti,*[a] Polina M. Sheverdyaeva,◇[a] Paolo Moras,[a] Carlo Carbone,[a] and Alexey N. Mihalyuk•[b,c]

Received Date
Accepted Date

DOI: 00.0000/xxxxxxxxxx

Dimensionality can strongly influence the magnetic structure of solid systems. Here, we predict theoretically and confirm experimentally that the antiferromagnetic (AFM) ground state of bulk gadolinium germanide metalloxene, which has a quasi-layered defective $GdGe_2$ structure, is preserved in the ultrathin film limit. *Ab initio* calculations demonstrate that ultrathin $GdGe_2$ films present in-plane intra-layer ferromagnetic coupling and AFM inter-layer coupling in the ground state. Angle-resolved photoemission spectroscopy finds the AFM-induced band splitting expected for the 2 and 3 $GdGe_2$ trilayer (TL) films, which disappear above the Néel temperature. The comparative analysis of isostructural ultrathin $DyGe_2$ and $GdSi_2$ films confirms the magnetic origin of the observed band splitting. These findings are in contrast with the recent report of ferromagnetism in ultrathin metalloxene films, which we ascribe to the presence of uncompensated magnetic moments.

1 Introduction

The scientific community working in the field of magnetism shows growing interest towards interfaces, surfaces and materials of reduced dimensionality[1]. As an example, the recently discovered two dimensional (2D) magnetic materials are now the focus of intensive research efforts[2]. In these layered compounds, including Fe_3GeTe_2 [3,4], $Cr_2Ge_2Te_6$ [5], CrI_3 [6,7], the ferromagnetic (FM) state is stabilized by the intrinsic anisotropy of the crystal structure that reduces the spin degree of freedom and allows to overcome the restriction of the Mermin-Wagner theorem[8]. They are an ideal experimental test environment for the verification of 2D magnetic phase-transition theories[9–11].

Another important research topic connected to the previous one is non-collinear magnetism, which gives rise to skyrmions, for instance[12–16]. Among the various compounds showing non-collinear magnetism, silicides and germanides of the 3*d* elements with the cubic B20 structure attracted remarkable attention[17]. The observation of extremely small skyrmions in the Gd-based inter-metallic compounds has also been reported[18,19].

The binary silicides and germanides of the rare-earth elements have been the subject of intense study since 1960s[20]. These compounds have a quasi-layered defective AlB_2 crystallographic structure in which honeycomb-like semiconductor layers are separated by rare-earth atomic layers (trilayer, TL). By analogy with materials containing honeycomb layers they are called metalloxenes. They can be epitaxially grown on the parent semiconductor substrates[21] to form hetero-structures with low Schottky-barrier heights[22]. Nowadays, due to growing interest in 2D and graphene-like structures, these systems are being revisited[23–27].

In the bulk most of the metalloxenes tend to be antiferromagnetic (AFM) with Néel temperatures (T_N) in the range of 10÷50 K[20]. For example, T_N =38 K and 54 K for Gd germanides[26] and silicides[28], respectively. Surprisingly, 2D FM order with magnetic moments in the order of 0.1 μ_B has been recently found in ultrathin metalloxenes films[26,27]. The 2D electron confinement could explain the experimental observation of the AFM to FM transition with decreasing the film thickness. However, the origin of this behavior has not been fully clarified and deserves further analysis.

In this regard, temperature-dependent angle-resolved photoemission spectroscopy (ARPES) is a powerful tool, since it remains sensitive to the deviations of band structure induced by magnetic order also in low-dimensional systems[29–33]. In particular, ARPES, in combination with *ab initio* density-functional calculations (DFT), can give a clue on the exact magnetic structure[34–36]. In the present study we investigate by ARPES and DFT the elec-

[a] *Istituto di Struttura della Materia-CNR (ISM-CNR), Strada Statale 14 km 163.5, 34149, Trieste, Italy*
[b] *Institute of Automation and Control Processes FEB RAS, 690041 Vladivostok, Russia*
[c] *Institute of High Technologies and Advanced Materials, Far Eastern Federal University, 690950 Vladivostok, Russia*
*E-mail: andrei.matetskii@trieste.ism.cnr.it
⋆E-mail: valeria.milotti@unipd.it. Present affiliation: Department of Physics and Astronomy "Galileo Galilei", University of Padua, Via F. Marzolo, 8, 35131 Padua, Italy
◇E-mail: polina.sheverdyaeva@ism.cnr.it
•E-mail: mih-alexey@yandex.ru
† Electronic Supplementary Information (ESI) available: [Interplay between magnetic order and electronic band structure in ultrathin $GdGe_2$ metalloxene films]. See DOI: 00.0000/00000000.

tronic and magnetic structure of Gd germanide metalloxene films grown on Ge(111). Our results show that the AFM order remains the ground state of the films down to the ultrathin limit of 2 and 3 TL. The FM order observed in Ref.[26] turns out to be caused by the presence of uncompensated magnetic moments in the order of 0.1 μ_B. These moments are found to derive from the hybridization of Gd 5*d* and Ge 4*p* levels in the low-symmetry film structure and/or are ascribed to the coexistence of multiple film thickness. ARPES data of Gd silicide and Dy germanide ultrathin metalloxene films are provided to strengthen our conclusions.

2 Experimental and calculation details

The experiments were performed at the VUV-Photoemission beamline at Elettra synchrotron (Trieste, Italy), by means of ARPES and low-energy electron diffraction (LEED) methods. The base pressure of the analysis and preparation chambers was $\leq 1.0\times10^{-10}$ Torr and $\leq$ and 3×10^{-10} Torr, respectively. The Ge(111) and Si(111) substrates were used for metalloxene films growth. The Ge(111) substrates were sputtered with Ar^+ ion bombardment and then annealed at 650°C; this procedure was repeated several times until the sharp c(2×8) LEED pattern was obtained. In order to obtain Si(111)7×7 surface reconstruction, Si(111) was flash annealed to a temperature of ∼1200°C. Gd and Dy were deposited using electron bombardment sources with rates of ∼0.25 ML/min [1 monolayer (ML) = 6.2×10^{14} cm^{-2} in terms of the Ge(111) surface atomic density]. The evaporation rate was calibrated by the observation of LEED patterns that correspond to known surface reconstructions: 5×2 at coverage < 1 ML, 1×1 that correspond to completion of the first TL at coverage ∼1 ML and $\sqrt{3}\times\sqrt{3}$ at coverage above 1 ML[21]. During deposition the substrates were held at ∼400°C. The Si substrates were annealed at ∼550-650°C after Gd deposition in order to improve the crystalline order of the films. It should be pointed out here that such procedure gives rise to films with multiple film thickness after the completion of 1 TL[21,23], as it will be shown while discussing the properties of the 2 TL films. ARPES measurements were conducted in the 14÷82 K temperature range using a Scienta R4000 electron analyzer and excitation energies between 25 eV and 150 eV with *p*-polarized light. The ARPES data shown in the article are taken with 35 eV photon energy that allowed for the best contrast of the features of interest. The electron spectrometer was placed at 45° with reference to the direction of the incoming photon beam. The labels of the high symmetry points in the ARPES spectra refer to the 1×1 surface Brillouin zone (BZ) of the substrates.

Calculations were based on DFT as implemented in the Vienna *ab initio* simulation package VASP.[37] The projector-augmented wave approach[38] was used to describe the electron-ion interaction and the generalized gradient approximation (GGA) of Perdew, Burke, and Ernzerhof (PBE)[39] was employed as the exchange-correlation functional. The scalar relativistic effect and the spin-orbit coupling (SOC) were taken into account. To simulate the $GdGe_2$, $DyGe_2$ and $GdSi_2$ structures we used a slab consisting of four bilayers (BL) of germanium/silicon with the PBE-optimized bulk lattice constants. Hydrogen atoms were used to passivate the dangling bonds at the bottom of the slab. The

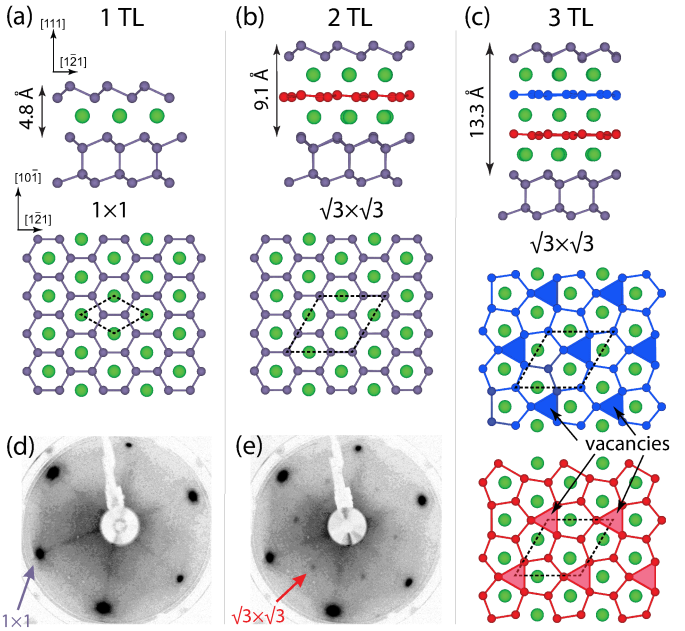

Fig. 1 (a-c) Side and top views of the relaxed atomic structure models of the $GdGe_2$ films with thickness of 1-3 TL placed on Ge(111) slab. Green balls correspond to Gd atoms while gray, red and blue balls correspond to Ge. Black dashed rhombuses outline the 1×1 and $\sqrt{3}\times\sqrt{3}$ unit cells. (d,e) LEED patterns measured for 1 and 2 TL $GdGe_2$ films, respectively.

atomic positions of adsorbed Gd/Dy atoms and atoms of upper Ge/Si layer and layers within the three BLs of the slab were optimized. Substrate atoms of the deeper layers were kept fixed at the bulk crystalline positions. The kinetic cutoff energy was 250 eV, and a 12×12×1 and 7×7×1 *k*-point meshes were used to sample the 1×1 and $\sqrt{3}\times\sqrt{3}$ supercell BZ, respectively. The geometry optimization was performed until the residual force on atoms was smaller than 10 meV/Å. For band-structure calculations, two types of Gd/Dy pseudopotentials were used[40]. The trivalent Gd/Dy potentials, where strongly localized, valence 4*f* electrons are treated as core states were used for non-magnetic band-structure calculations. In order to describe the magnetic properties, the standard Gd/Dy potentials were used for spin-polarized non-collinear calculations, in which the *f* electrons are treated as valence states. The Heyd-Scuseria-Ernzerhof (HSE06) screened hybrid functional was used to accurately calculate the Ge gap and to avoid the self-interaction errors arising from an incorrect description of partially filled *f* states of Gd/Dy[41].

3 Results and Discussion

3.1 Atomic structure of the ultrathin $GdGe_2$ films

Trivalent rare-earth elements form germanides and silicides of various stoichiometries[20]. In the present paper we will study defective $AlB2_2$ type ultrathin Gd germanide metalloxene films. Figure 1(a-c) shows the relaxed crystallographic structures of 1-3 TL films on Ge(111) obtained by the *ab initio* random structure searching (AIRSS) method[42]. The atomic structure of the 1 TL $GdGe_2$ (Fig. 1(a)) corresponds to the one reported previously in the literature[23,26,43]. It consists of a single layer of Gd atoms sandwiched between the Ge(111) substrate and the buckled Ge

surface bilayer (BL). This BL displays a reversed buckling with respect to the substrate. The 1 TL system has $GdGe_2$ stoichiometry, hexagonal symmetry and 1×1 LEED pattern (Fig. 1(d)).

The formation of films thicker than 1 TL reduces the symmetry of the surface from hexagonal to trigonal and changes the surface periodicity from 1×1 to $\sqrt{3}\times\sqrt{3}$[23], as demonstrated by the emergence of weak $\sqrt{3}\times\sqrt{3}$ reflexes in the LEED pattern (Fig. 1(e)). This weak periodicity was connected with the formation of the vacancy lattice in the inner semiconductor BLs of metalloxenes[44]. Due to these vacancies the Ge BLs become almost flat (red and blue balls in Figs. 1(b, c)) and the overall stoichiometry of the inner TLs becomes Gd_3Ge_5. In spite of this change, for convenience we will use the $GdGe_2$ notation for all Gd germanide films (we will adopt a similar nomenclature for Gd silicide and Dy germanide films), irrespectively of their thickness.

According to our calculations, the Gd atoms of the different layers are always located at the T_4 site with reference to the underlying Ge(111) substrate. This is in line with previous high-angle annular dark-field transmission electron microscopy observations[25,26]. The geometry of the topmost Ge BL is the following: the upper Ge atom is located in the T_1 site, while the lower Ge atom is located in the H_3 site. For the 2 TL system the most energetically stable atomic configuration of the intermediate flat Ge layer has a vacancy defect located in one of the T_1 sites. Importantly, the vacancy defects within flat Ge layers in 3 TL and thicker films have alternating positions with respect to the neighboring Ge layers, as shown in Fig. 1(c). The total thicknesses of 1, 2 and 3 TL $GdGe_2$ films is 4.8, 9.1, and 13.3 Å, respectively.

3.2 Thickness-dependent electronic band structure of the $GdGe_2$ films in the paramagnetic phase

In this section we show ARPES data and DFT calculations for $GdGe_2$ films of different thickness. The ARPES spectra and Fermi surfaces for 1, 2, 3 and 9 (nominal) TL are shown in Figs. 2(a-g). Colored arrows and S1-S3 labels mark the characteristic features in the band structure that allow the identification of the film thickness and are discussed below in connection with the magnetic properties. The electronic structure of 1 TL (Fig. 2(a)) consists in the highly dispersive S1 surface band. This band is reproduced well by the DFT calculations for the 1 TL $GdGe_2$ model previously discussed in section 3.1 (DFT results are shown in Fig. S1(a) of the Electronic Supplementary Information (ESI) and overlaid onto the ARPES data in Fig. 2(a)). The Gd-Ge hybridization leads to the formation of the camel-like feature at the top of the S1 band, which touches the Fermi level and forms a ring-like hole pocket around the $\bar{\Gamma}$ point (Fig. 2(e)).

The 2 TL $GdGe_2$ film (Fig. 2(b)) shows a S1 hole-like band similar to the 1 TL case. With respect to 1 TL, it is shifted to slightly higher binding energies at $\bar{\Gamma}$ and by 0.5 eV towards lower energies at the $\bar{M}$ point and is fully occupied. Additionally, a new S2 band leads to the formation of the electron pocket around the $\bar{M}$ points (Figs. 2(b,f)). The dispersion of these states is in a good agreement with the DFT predicted band structure of 2 TL shown in Fig. S1(b) of ESI and in Fig. 3(f). In turn, a number of intense features is associated with higher thicknesses due to the inhomogeneous sample growth. A metallic band labeled $S1^*$ is observed along the $\bar{\Gamma}-\bar{M}$ direction. According to the calculation in Fig. S1(c) of the ESI and Fig. 4(e) it is associated to the 3 TL film and, therefore, is a manifestation of the coexistence of multiple thickness above the completion of 1 TL. Further confirmation of this assignment comes from the fact that at the nominal coverage of 3 TL the intensity of the S1 band, whose dispersion coincides with $S1^*$, is much stronger (Fig. 2(c)). Similarly, a strong intensity observed at $\bar{\Gamma}$ close to 0.3 eV derives from 3 TL thick sample (violet arrow), in agreement with DFT (Fig. S1(c) of ESI), while the intense parabolic feature at 0.8 eV (green arrow) derives from thicker films as it becomes most prominent in Fig. 2(d). In addition to the S1 and S2 bands, the proximity of the Fermi level of the 3 TL films is characterized by a weak electron pocket labeled S3 observed between $\bar{\Gamma}$ and $\bar{M}$ (Fig. 2(c)). Close to 0.5 eV at $\bar{M}$ a faint cone-like feature can be observed in Figs. 2(b,c). Its upper branch corresponds to the 2 TL film, while the lower one, that becomes more intense in Fig. 2(c), corresponds to 3 TL film (see Section 2 of ESI for more details).

In thicker films (Figs. 2(d, g)) the spectrum in the vicinity of Fermi level is characterized by the presence of electron-like bands near the $\bar{M}$ point and hole-like bands near the $\bar{\Gamma}$ point. The apex of the cone-like band in $\bar{M}$ point shifts towards lower binding energies with thickness and start to hybridize with the S2-like bands. This feature follows the vacancy-associated super-periodicity and can be found also in $\bar{M}_{\sqrt{3}}$ points (Fig. 2(h)). Therefore, while the hole pockets around the $\bar{\Gamma}$ point and electron pockets in the $\bar{M}$ points remain dominant, the spectral intensities in thicker films display additional features associated with the $\sqrt{3}\times\sqrt{3}$ lattice which may be seen in the ARPES plot and Fermi surface map (Fig. 2(g)).

3.3 Transition temperature and magnetic order of the $GdGe_2$ films

In order to study the magnetic order and the effect of magnetism on the electronic structure of the $GdGe_2$ films, we performed comprehensive *ab initio* calculations. The magnetic ground state of the Gd germanide system was determined by calculating the total energies for various magnetic configurations (see Tab. 1). Collinear in-plane AFM (cl $AFM_{\parallel}$) represent the ground state for the multilayered films. The out-of-plane collinear AFM (cl $AFM_{\perp}$) configuration is less favorable by 0.2 meV per Gd atom. While the difference in total energy between cl $AFM_{\parallel}$ and cl $AFM_{\perp}$ is small it is enough to judge on magnetic ground state. The in-plane non-collinear 120° AFM (ncl 120° $AFM_{\parallel}$) has 5 meV higher energy than the ground state. Finally, the in-plane FM ($FM_{\parallel}$) and out-of-plane FM ($FM_{\perp}$) configurations are much less favorable than cl $AFM_{\parallel}$. For 1 TL $GdGe_2$ film, $FM_{\parallel}$ is the ground state and is lower than $FM_{\perp}$ by 0.5 meV.

Let us now examine the effect of magnetism on the electronic band structure of the $GdGe_2$ films by temperature-dependent ARPES and magnetic DFT calculations. We did not find any evidence of the magnetic behavior in the 1 TL $GdGe_2$ film down to ~14 K. We did not observe any magnetically-induced splitting of the S1 surface band or any other band structure changes,

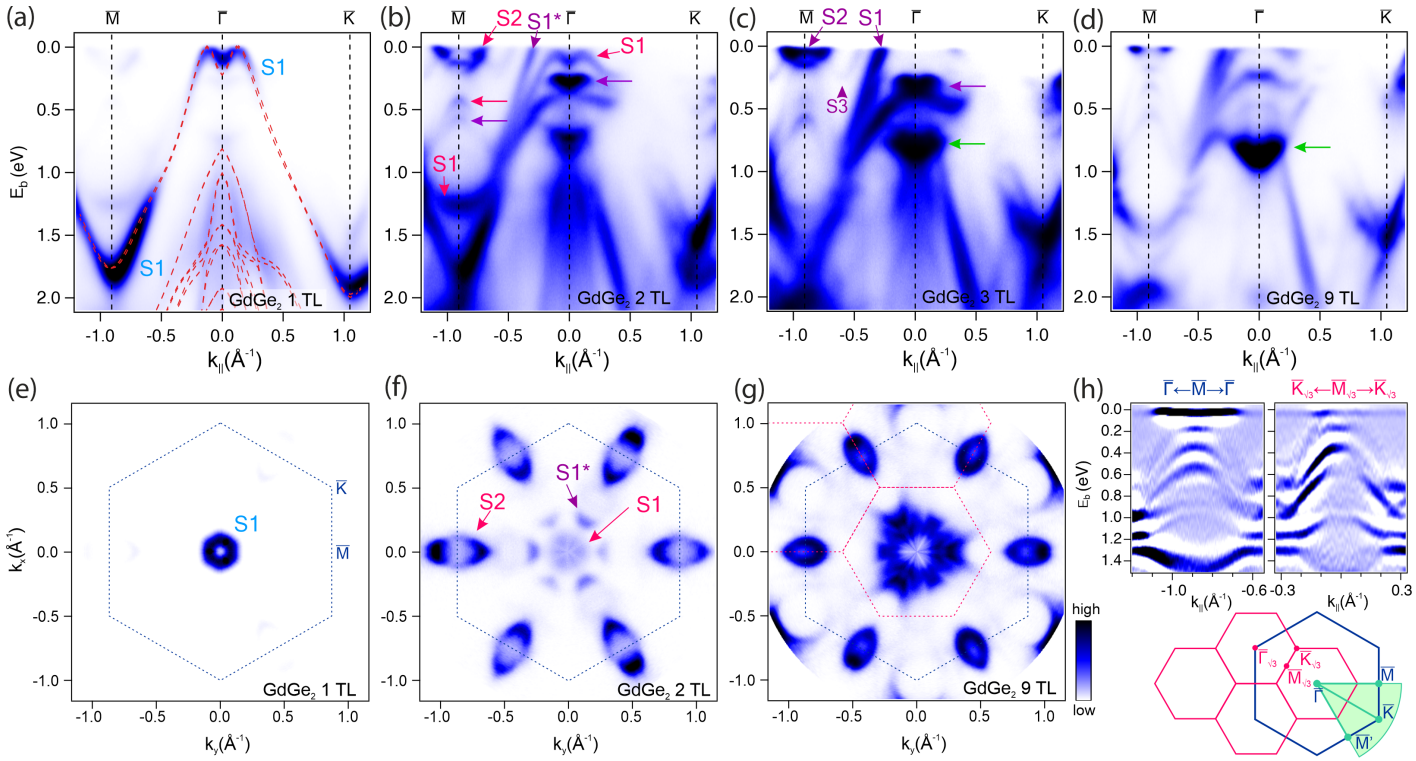

Fig. 2 (a-d) ARPES spectra of $GdGe_2$ films with thicknesses of 1, 2, 3 and 9 TL, respectively. All spectra are taken at 82 K with 35 eV photon energy. In (a) the results of DFT calculation for 1 TL $GdGe_2$ are overlaid on the ARPES data with adjusted Fermi level. (e-g) Fermi surface maps of $GdGe_2$ films with thicknesses of 1, 2 and 9 TL, respectively. The color of the labels S1, S2 and S3 indicates a specific film thickness: blue - 1 TL, red - 2 TL, violet - 3 TL, green - thick films. (h) Top: second derivatives of the ARPES spectra in the vicinity of $\bar{M}$ and $\bar{M}_{\sqrt{3}}$ points. Bottom: schematics of the surface BZs for the 1×1 and $\sqrt{3}\times\sqrt{3}$ lattices and ARPES measurement geometry. Teal lines mark the direction for the experimental measurements in (a-d). The teal sector depicts the azimuthal scan used to obtain the Fermi surfaces in (e-g).

cl $AFM_{\parallel}$	cl $AFM_{\perp}$	ncl 120° $AFM_{\parallel}$	$FM_{\parallel}$	$FM_{\perp}$
0.0	0.2	5.0	10.0	11.0

Table 1 Energies (meV/Gd atom) of different magnetic configurations of the 2 TL $GdGe_2$ film with respect to the ground state. Energies for films of higher thicknesses follow similar trend. [collinear in-plane AFM (cl-$AFM_{\parallel}$), collinear out-of-plane AFM (cl-$AFM_{\perp}$); non-collinear 120° AFM (ncl 120° $AFM_{\parallel}$), in-plane FM ($FM_{\parallel}$), out-of-plane FM ($FM_{\perp}$)]

which were predicted by the band structure calculations in the $FM_{\parallel}$ phase (Fig. S1, ESI). Therefore we came to the conclusion that the Curie temperature for the 1 TL lays below 14 K, in line with the magnetic measurements [45].

We made a temperature-dependent ARPES measurements for the 2 TL $GdGe_2$ across the transition temperature reported in Ref. [26] and investigated the behavior of the S1 and S2 bands. Figures 3(a, b) show the experimental spectra recorded at 14 and 82 K, respectively. At 14 K the S1 band displays a magnetic spin splittings of ≈130 meV at the $\bar{\Gamma}$ point just below the Fermi level and of ≈100 meV at the $\bar{M}$ point at E_b ≈1.25 eV. Both splittings can be resolved in the second derivative spectra shown in Fig. 3(c). When the temperature is raised up to 82 K, the above mentioned spin splittings at $\bar{\Gamma}$ and $\bar{M}$ disappear, while a tiny k-dependent splitting can still be observed near the $\bar{\Gamma}$ point (Fig. 3(c)). The cone-like feature deriving from 2 TL film (red arrow) shows a tiny shift towards lower binding energies at $\bar{M}$ and its splitting can be better resolved in a different experimental geometry (see Section 2 of ESI for more details). Instead, the S2 state does not show any significant change with temperature, in line with the DFT predictions. Thus, to track the magnetic transition of the 2 TL film we use the temperature dependence of the splitting of the S1 state near the $\bar{\Gamma}$ point. According to ARPES measurements made within the [14÷45] K temperature range the Néel transition temperature in 2 TL $GdGe_2$ film is 31±1 K (fitting results for the exchange splitting value in Fig. S3 of ESI are deduced from energy distribution curves in Fig. 3(d)). This indicates that already at the thickness of 2 TLs the $GdGe_2$ film has a transition temperature that is close to the bulk value [20].

The unfolded band structure calculations for the cl $AFM_{\parallel}$ and non-magnetic phases are shown in Figs. 3(e, g) and Figs. 3(f, h), respectively, while the band structure for the ncl 120° $AFM_{\parallel}$ phase is shown in Fig. 3(i). The band structure calculation for the cl $AFM_{\perp}$ and $FM_{\perp}$ are shown in Fig. S4. It should be noted that the unfolding procedure [46,47] was used for comparison of the experimental and calculated band structures, since collinear and ncl 120° $AFM_{\parallel}$ band structure calculations require different unit cells. Namely, the cl $AFM_{\parallel}$ and non-magnetic band structures initially calculated within the 3×3 and $\sqrt{3}\times\sqrt{3}$ supercells, respectively, were then unfolded onto the 1×1 surface BZ. DFT calculations for cl $AFM_{\parallel}$ configuration (Fig. 3(e)) perfectly reproduce the

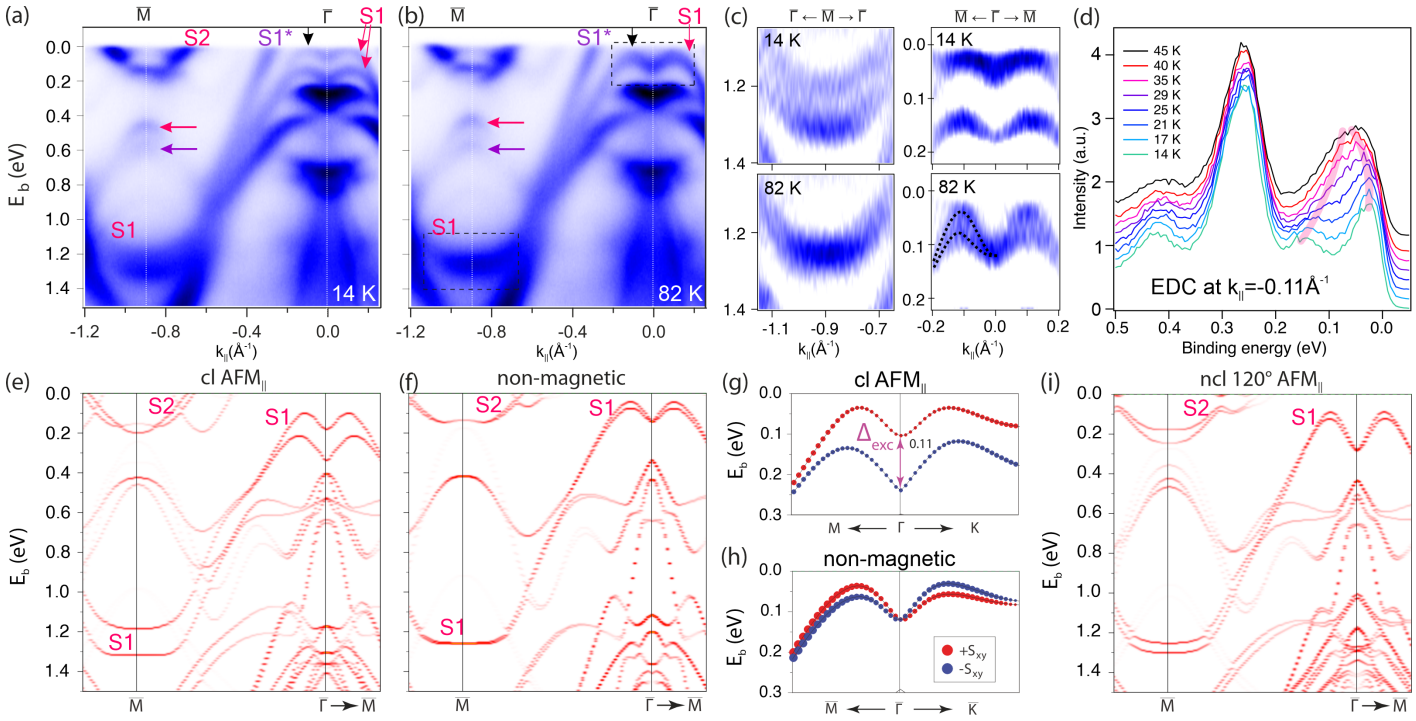

Fig. 3 Electronic structure of the 2 TL $GdGe_2$ film. (a, b) ARPES spectra taken at 14 K and 82 K, respectively, with 35 eV photon energy. The color of the labels S2 and S3 and arrows indicates a specific film thickness: red - 2 TL, violet - 3 TL. (c) Second derivatives of the ARPES spectra in the vicinity of $\bar{\Gamma}$ and $\bar{M}$ points (marked by dashed rectangular in (b)) at 14 K (top row) and 82 K (bottom row). (d) Energy distribution curves taken at the top of the S1 band ($k_{||}$=0.11 Å^{-1}, black arrows in (a, b)) in the temperature range 14÷45 K. The pink lines highlight the change of the two spin-split bands with the temperature. These bands do not overlap above T_N due to the Rashba effect. (e, f) DFT electronic structure calculations for 2 TL $GdGe_2$ with cl $AFM_{||}$ and non-magnetic configurations, respectively. The bands are unfolded onto the 1×1 surface BZ to be easily compared with the ARPES data. (g, h) Zoom of panels (e, f) near the top of the S1 band. Red and blue colors represent the opposite in-plane spin components. (i) DFT electronic structure calculations for 2 TL $GdGe_2$ with ncl 120° $AFM_{||}$ order unfolded onto the 1×1 surface BZ.

low-temperature features of the experimental electron dispersion (Fig. 3(a)). The magnitude of the calculated exchange splitting of the S1 band at the $\bar{\Gamma}$ point is equal to 110 meV (Figs. 3(e, g)), which is very close to the ARPES observation of $\Delta \approx$130 meV at 14 K. Similarly, the calculated splitting of the S1 band at the $\bar{M}$ point is 130 meV (Fig. 3(e)) which is also close to the ARPES-derived value ($\Delta \approx$100 meV). The energy splittings predicted by DFT for the S2 state and for the cone-like feature at $\bar{M}$ are difficult to resolve by ARPES due to low intensity and a significant overlap with the 3 TL-derived features (see Fig. S2 of ESI). The calculation for the non-magnetic case (Gd 4f orbitals are treated as core states) reproduces perfectly the experimental observation at temperatures above the magnetic transition (Fig. 3(f)). The S1 band demonstrates a Rashba-like spin splitting[48] in the vicinity of the $\bar{\Gamma}$ point with vortical spin-texture (Fig. 3(h)). This Rashba-like spin splitting can be observed in the second derivative of 82 K ARPES spectrum in Fig. 3(c). Instead, the band structure for the ncl 120° $AFM_{||}$ magnetic configuration (Fig. 3(i)) does not show any significant exchange splitting for the S1 band at the $\bar{\Gamma}$ point. This supports the total energy calculation results that ncl 120° $AFM_{||}$ magnetic configuration is not a ground state. The band structure calculated for the $FM_{\perp}$ magnetic configuration (Fig. S4(a) of ESI) does not fit the experimental results as it shows three times higher splitting values that are not k-dependent. In turn, the band structure calculated for the $AFM_{\perp}$ magnetic configuration (Fig. S4(b) of ESI) is almost identical to one of $AFM_{||}$. However, the camel-like feature at $\bar{\Gamma}$ is shifted to lower binding energies and has a smaller splitting in the case of $AFM_{\perp}$ that is less consistent with the experimental observations.

Interestingly, the energy position of the exchange-split camel-like feature at $\bar{\Gamma}$ varies strongly with thickness. In the 3 TL $GdGe_2$ film it is located above the Fermi level (Figs. 4(a,d)) and the S1 band is not fully occupied, in contrast to the 2 TL $GdGe_2$ film. The magnetic transition here can still be traced experimentally by analyzing the band structure evolution with temperature. The S3 band forms an electron pocket between $\bar{\Gamma}$ and $\bar{M}$ points with a minimum at $k_{||}$=0.6 Å^{-1} and exhibits exchange splitting: in the 14 K data there are two pockets separated by 270 meV with the lower branch minimum at 340 meV (Fig. 4(a)), while in the 82 K data there is single pocket with the minimum at 250 meV (Fig. 4(b)). The S3 band behavior in $k_{||}$=0.6 Å^{-1} can be better visualized in the top panel of Fig. 4(c). Another difference between the low and high temperature spectra is the appearance of a faint intensity at the Fermi level near the $\bar{\Gamma}$ point at 14 K that can be connected with the dip of the S1 band (bottom panel of Fig. 4(c)). The behavior of these features at $\bar{\Gamma}$ and $k_{||}$=0.6 Å^{-1} is well reproduced by the calculations for the cl $AFM_{||}$ and non-magnetic phases (Figs. 4(d,e)), in close analogy to the case of the 2 TL films. Also for the 3 TL film the quenching of the exchange splitting of the S1 band near $\bar{\Gamma}$ is accompanied by the appearance of Rashba-

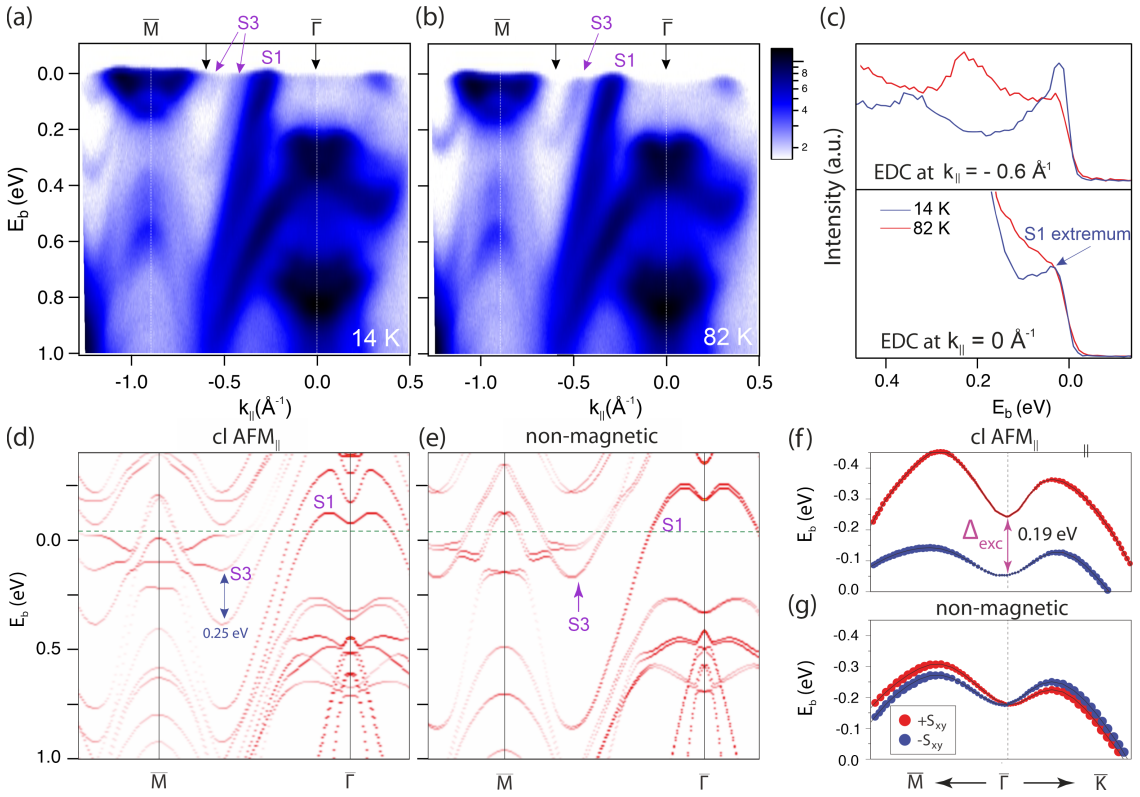

Fig. 4 Electronic structure of the 3 TL $GdGe_2$ film. (a, b) ARPES spectra recorded at 14 K and 82 K, respectively, taken with 35 eV photon energy. A logarithmic intensity scale is used to highlight weak features. (c) Energy distribution curves taken at $k_{||}$=0.6 Å^{-1} and $\bar{\Gamma}$ from the ARPES data of panel (a, b). (d, e) DFT calculations for the 3 TL $GdGe_2$ film for cl $AFM_{||}$ and non-magnetic phases, respectively. The bands are unfolded onto the 1×1 surface BZ to ease the comparison with the ARPES spectra. (f, g) Zoom of panels (d, e) near the top of the S1 band. Red and blue colors represent the opposite in-plane spin components.

split bands with vortical spin-texture (Figs. 4(f,g)). The experimental observation of the cone-like states splitting predicted by the calculations is hindered in the case of 3 TL films by weak spectral intensity of this features and sample thickness inhomogeneity (see Section 2 of ESI for more details).

Notably, we did not observe explicit fingerprints of magnetic transition in the valence band structure of ultrathin $DyGe_2$ and $GdSi_2$ metalloxene films, which have the same crystallography structure of the $GdGe_2$ films (Fig. S5 of ESI). $DyGe_2$ and $GdGe_2$ show nearly identical band structures. Consistently with the fact that bulk Dy_3Ge_5 has T_N=7 K, our measurements on the 2 TL $DyGe_2$ film at 14 K do not reveal any magnetically-induced band splitting. The band structure of the 2 TL $GdSi_2$ film presents the same features of the corresponding $GdGe_2$ film, with the only notable difference being the parabolic top of the S1 band at the $\bar{\Gamma}$ point. Despite bulk Gd_3Si_5 has T_N=54 K[28], which is higher than the value for bulk Gd_3Ge_5 (T_N=38 K), the ARPES data for the 2 TL $GdSi_2$ film do not display any signature of magnetically-induced band splitting. This behavior can be ascribed to the non-collinear AFM ground state of Gd_3Si_5[28], which is likely to have only minor influence on the band structure, as shown for the ncl 120° $AFM_{||}$ configuration of the 2 TL $GdGe_2$ film (Fig. 3(i)).

Spin-splitting observed for the electronic bands in the 2 and 3 TL $GdGe_2$ films in $AFM_{||}$ phase is originated from the surface associated relaxation and inversion symmetry breaking. AFM materials with reduced symmetry often show splitting of the Pekar-Rashba type[49–51]. Also, surface states, in particular, S1 state has a localization centered in a proximity to the subsurface magnetic atoms (Fig. S1(d) of ESI) and hence predominantly couples to the magnetic moment of the topmost Gd layer, that drives the exchange splitting of the surface state[31,33]. These surface effects can alter the magnetic properties, as we show in the next subsection.

3.4 Uncompensated magnetic moments in AFM $GdGe_2$ films

As a final remark we want to address the discrepancy of our results with previously reported FM behavior in ultrathin metalloxene films[26]. The 2 TL AFM $GdGe_2$ film can display an uncompensated magnetic moment induced by orbital hybridization of Gd and Ge atoms. Indeed, the S1 band that exhibits the largest splitting in the vicinity of the Fermi level in the AFM state is localized on both Gd and surrounding Ge atoms (Fig. S1(d) of ESI). As shown in Tab. 2 the expectation value of the spin moment (S) of the first Gd layer is -21.125 μ_B, while S of the second Gd layer equals to 21.195 μ_B resulting in a small residual magnetic moment of 0.070 μ_B. The Ge BL residing on top of the structure provides 0.184 μ_B mostly from its p orbitals. Contribution from other Ge layers including those of the substrate is opposite leading to total magnetic moment from all Ge atoms of 0.111 μ_B. Overall, the contribution from Gd and Ge atoms results in a net

Atomic layers	N_A	p-	d-	f-	Total	Total per atom
Ge top BL	6	0.187	–0.003	0.000	0.184	0.030
Gd 1st layer	3	0.030	–0.404	–20.751	–21.125	7.042
Ge inner layer	5	–0.007	0.005	0.000	–0.002	0.000
Gd 2nd layer	3	–0.027	0.465	20.757	21.195	7.065
Ge(111) 1st BL	6	–0.057	0.006	0.000	–0.051	–0.017
Ge(111) 2nd BL	6	–0.020	0.000	0.000	–0.020	–0.007
Total	29	0.106	0.069	0.006	0.181	0.006

Table 2 Layer-decomposed representation of spin magnetic moments S (μ_B) for Gd and Ge atoms estimated within 2 TL $GdGe_2$ film with cl $AFM_{\|}$ magnetic ordering (see Fig. 1(b) for reference). The column depicted as N_A shows the number of atoms per each atomic layer. The columns denoted p-, d- and f- provide the total magnetic moment per atomic layer. The last column shows S values per N_A, *i.e.* magnetic moment per atom.

positive magnetic moment of 0.181 μ_B, or 0.030 μ_B per Gd atom. Considering the magnetic moment of interstitial regions and the *s* orbitals of Ge atoms, the total integrated magnetic moment for the structure shown in Fig. 1(b) results in 0.495 μ_B total magnetic moment, or 0.085 μ_B per Gd atom. This tiny but non-zero value is in line with the small magnetic moment (compared to that of elemental Gd) reported in the magnetic measurements for 2 TL thick metalloxene films[26]. Another possible explanation for the reported FM behavior is the unavoidable inhomogeneity of the sample thickness that we observed directly in our samples and that was previously noticed in the scanning tunneling microscopy analysis of metalloxene films[21,23]. Space averaging investigation techniques, such as superconducting quantum interference device, can pick up signals from different film thickness while only areas of odd number of layers will contribute to the signal. This would explain the relatively low magnetic moments observed for the films of odd number of layers[26].

4 Conclusions

Our study of ultrathin rare-earth $GdGe_2$ metalloxenes films by ARPES measurements and comprehensive *ab initio* calculations shows in-plane FM order inside the single TL and AFM interlayer coupling. The hybridization between Gd and Ge orbitals induces a small uncompensated magnetic moment in the AFM-ordered films, which was previously associated with a FM ground state for these systems. The observed evolution of the $GdGe_2$ band structure with thickness suggests that exchange-split bands can be tuned in a broad energy range, thus providing a viable way to design the magnetic properties of the films, also through the well-known doping techniques of semiconductor technology. Another interesting way to tune the magnetism in such systems is the incorporation of the metalloxene magnetic layers within semiconductor hetero-structures[52], which makes them promising candidates for 2D materials engineering, similar to that proposed for layered chalcogenides. Finally, the spin *S*, orbital *L* and total magnetic momenta *J* of the metalloxenes can be controlled by suitable choice of rare-earth elements that have similar valence states and ionic radius. All these aspects make metalloxens a convenient playground to study magnetism in the 2D limit.

Author Contributions

A. V. Matetskiy: Investigation, Conceptualization, Supervision, Writing - original draft, Writing - Review and Editing, Project administration. V. Milotti: Investigation, Formal analysis, Writing - Review and Editing. P. M. Sheverdyaeva: Investigation, Validation, Writing - Review and Editing. P. Moras: Investigation, Validation, Writing - Review and Editing. C. Carbone: Validation, Conceptualization. A. N. Mihalyuk: Software, Conceptualization, Visualization, Writing - original draft, Writing - Review and Editing.

Conflicts of interest

There are no conflicts to declare.

Acknowledgements

A. N. Mihalyuk acknowledge that DFT calculations were supported by the Russian Science Foundation (Grant No. 19-12-00101, `https://rscf.ru/project/19-12-00101/`). A. V. Matetskiy, P. M. Sheverdyaeva, P. Moras, C. Carbone acknowledge EUROFEL-ROADMAP ESFRI of the Italian Ministry of Education, University, and Research. The authors thank S.V. Eremeev for comments and helpful discussions. The calculations were conducted using the equipment of Shared Resource Center "Far Eastern Computing Resource" IACP FEB RAS (https://cc.dvo.ru).

References

1 E. Vedmedenko, R. Kawakami, D. Sheka, P. Gambardella, A. Kirilyuk, A. Hirohata, C. Binek, O. Chubykalo-Fesenko, S. Sanvito, B. Kirby, J. Grollier, K. Everschor-Sitte, T. Kampfrath, C.-Y. You and A. Berger, *Journal of Physics D: Applied Physics*, 2020, **53**, 1–44.

2 X. Jiang, Q. Liu, J. Xing, N. Liu, Y. Guo, Z. Liu and J. Zhao, *Applied Physics Reviews*, 2021, **8**, 031305.

3 K. S. Burch, D. Mandrus and J. G. Park, *Nature*, 2018, **563**, 47–52.

4 Z. Fei, B. Huang, P. Malinowski, W. Wang, T. Song, J. Sanchez, W. Yao, D. Xiao, X. Zhu, A. F. May, W. Wu, D. H. Cobden, J. H. Chu and X. Xu, *Nature Materials*, 2018, **17**, 778–782.

5 C. Gong, L. Li, Z. Li, H. Ji, A. Stern, Y. Xia, T. Cao, W. Bao, C. Wang, Y. Wang, Z. Q. Qiu, R. J. Cava, S. G. Louie, J. Xia and X. Zhang, *Nature*, 2017, **546**, 265–269.

6 M. A. McGuire, H. Dixit, V. R. Cooper and B. C. Sales, *Chemistry of Materials*, 2015, **27**, 612–620.

7 B. Huang, G. Clark, E. Navarro-Moratalla, D. R. Klein, R. Cheng, K. L. Seyler, D. Zhong, E. Schmidgall, M. A. McGuire, D. H. Cobden, W. Yao, D. Xiao, P. Jarillo-Herrero and X. Xu, *Nature*, 2017, **546**, 270–273.

8 M. Gibertini, M. Koperski, A. F. Morpurgo and K. S. Novoselov, *Nature Nanotechnology*, 2019, **14**, 408–419.

9 R. Peierls, *Mathematical Proceedings of the Cambridge Philosophical Society*, 1936, **32**, 477–481.

10 N. D. Mermin and H. Wagner, *Physical Review Letters*, 1966, **17**, 1133–1136.

11 P. C. Hohenberg, *Physical Review*, 1967, **158**, 383–386.

12 H. Zhang, D. Raftrey, Y. T. Chan, Y. T. Shao, R. Chen, X. Chen, X. Huang, J. T. Reichanadter, K. Dong, S. Susarla, L. Caretta, Z. Chen, J. Yao, P. Fischer, J. B. Neaton, W. Wu, D. A. Muller, R. J. Birgeneau and R. Ramesh, *Science Advances*, 2022, **8**, 1–11.

13 C. Liu, Y. Wang, H. Li, Y. Wu, Y. Li, J. Li, K. He, Y. Xu, J. Zhang and Y. Wang, *Nature Materials*, 2020, **19**, 522–527.

14 Z. Ying, S. Zhang, B. Chen, B. Jia, F. Fei, M. Zhang, H. Zhang, X. Wang and F. Song, *Physical Review B*, 2022, **105**, 1–6.

15 Y. Deng, Y. Yu, M. Z. Shi, Z. Guo, Z. Xu, J. Wang, X. H. Chen and Y. Zhang, *Science*, 2020, **367**, 895–900.

16 J. Ge, Y. Liu, J. Li, H. Li, T. Luo, Y. Wu, Y. Xu and J. Wang, *National Science Review*, 2020, **7**, 1280–1287.

17 Y. Tokura and N. Kanazawa, *Chemical Reviews*, 2021, **121**, 2857–2897.

18 T. Kurumaji, T. Nakajima, M. Hirschberger, A. Kikkawa, Y. Yamasaki, H. Sagayama, H. Nakao, Y. Taguchi, T. Arima and Y. Tokura, *Science*, 2019, **365**, 914–918.

19 N. D. Khanh, T. Nakajima, X. Yu, S. Gao, K. Shibata, M. Hirschberger, Y. Yamasaki, H. Sagayama, H. Nakao, L. Peng, K. Nakajima, R. Takagi, T. Arima, Y. Tokura and S. Seki, *Nature Nanotechnology*, 2020, **15**, 444–449.

20 E. F. Westrum, *Progress in the Science and Technology of the Rare Earths*, Pergamon press, 1968.

21 I. Engelhardt, C. Preinesberger, S. Becker, H. Eisele and M. Dähne, *Surface Science*, 2006, **600**, 755–761.

22 S. Vandré, T. Kalka, C. Preinesberger and M. Dähne-Prietsch, *Phys. Rev. Lett.*, 1999, **82**, 1927–1930.

23 M. Wanke, M. Franz, M. Vetterlein, G. Pruskil, B. Höpfner, C. Prohl, I. Engelhardt, P. Stojanov, E. Huwald, J. Riley and M. Dähne, *Surface Science*, 2009, **603**, 2808–2814.

24 M. Franz, S. Appelfeller, C. Prohl, J. Große, H.-F. Jirschik, V. Füllert, C. Hassenstein, Z. Diemer and M. Dähne, *Journal of Vacuum Science & Technology A*, 2016, **34**, 061503.

25 O. E. Parfenov, A. M. Tokmachev, D. V. Averyanov, I. A. Karateev, I. S. Sokolov, A. N. Taldenkov and V. G. Storchak, *Materials Today*, 2019, **29**, 20–25.

26 A. M. Tokmachev, D. V. Averyanov, A. N. Taldenkov, O. E. Parfenov, I. A. Karateev, I. S. Sokolov and V. G. Storchak, *Materials Horizons*, 2019, **6**, 1488–1496.

27 D. V. Averyanov, I. S. Sokolov, M. S. Platunov, F. Wilhelm, A. Rogalev, P. Gargiani, M. Valvidares, N. Jaouen, O. E. Parfenov, A. N. Taldenkov, I. A. Karateev, A. M. Tokmachev and V. G. Storchak, *Nano Research*, 2020, **13**, 3396–3402.

28 J. Roger, V. Babizhetskyy, K. Hiebl, J. F. Halet and R. Guérin, *Journal of Alloys and Compounds*, 2006, **407**, 25–35.

29 C. Schüßler-Langeheine, E. Weschke, C. Mazumdar, R. Meier, A. Y. Grigoriev, G. Kaindl, C. Sutter, D. Abernathy, G. Grübel and M. Richter, *Phys. Rev. Lett.*, 2000, **84**, 5624–5627.

30 S. Pakhira, A. K. Kundu, F. Islam, M. A. Tanatar, T. Roy, T. Heitmann, T. Yilmaz, E. Vescovo, M. Tsujikawa, M. Shirai, R. Prozorov, D. Vaknin and D. C. Johnston, *Phys. Rev. B*, 2023, **107**, 134439.

31 A. Chikina, M. Höppner, S. Seiro, K. Kummer, S. Danzenbächer, S. Patil, A. Generalov, M. Güttler, Y. Kucherenko, E. V. Chulkov, Y. M. Koroteev, K. Köpernik, C. Geibel, M. Shi, M. Radovic, C. Laubschat and D. V. Vyalikh, *Nature Communications*, 2014, **5**, 1–7.

32 M. Schmitt, P. Moras, G. Bihlmayer, R. Cotsakis, M. Vogt, J. Kemmer, A. Belabbes, P. M. Sheverdyaeva, A. K. Kundu, C. Carbone, S. Blügel and M. Bode, *Nature Communications*, 2019, **10**, 1–6.

33 H. J. Elmers, S. Haldar, K. Medjanik, S. Babenkov, O. Fedchenko, D. Vasilyev, S. Heinze and G. Schönhense, *Phys. Rev. B*, 2023, **107**, 144424.

34 K. Lee, N. H. Jo, L.-L. Wang, R. A. Ribeiro, Y. Kushnirenko, B. Schrunk, P. C. Canfield and A. Kaminski, *Journal of Physics: Condensed Matter*, 2023, **35**, 245501.

35 S. V. Eremeev, D. Glazkova, G. Poelchen, A. Kraiker, K. Ali, A. V. Tarasov, S. Schulz, K. Kliemt, E. V. Chulkov, V. S. Stolyarov, A. Ernst, C. Krellner, D. Y. Usachov and D. V. Vyalikh, *Insight into the electronic structure of the centrosymmetric skyrmion magnet $GdRu_2Si_2$*, 2023.

36 L. Fernandez, M. Blanco-Rey, R. Castrillo-Bodero, M. Ilyn, K. Ali, E. Turco, M. Corso, M. Ormaza, P. Gargiani, M. A. Valbuena, A. Mugarza, P. Moras, P. M. Sheverdyaeva, A. K. Kundu, M. Jugovac, C. Laubschat, J. E. Ortega and F. Schiller, *Nanoscale*, 2020, **12**, 22258–22267.

37 G. Kresse and J. Hafner, *Physical Review B*, 1993, **47**, 558–561.

38 P. E. Blöchl, *Physical Review B*, 1994, **50**, 17953–17979.

39 J. P. Perdew, K. Burke and M. Ernzerhof, *Physical Review Letters*, 1996, **77**, 3865–3868.

40 G. Kresse and D. Joubert, *Physical Review B*, 1999, **59**, 1758–1775.

41 A. V. Krukau, O. A. Vydrov, A. F. Izmaylov and G. E. Scuseria, *The Journal of Chemical Physics*, 2006, **125**, 224106.

42 C. J. Pickard and R. J. Needs, *Journal of physics. Condensed matter*, 2011, **23**, 053201.

43 S. Sanna, J. Plaickner, K. Holtgrewe, V. M. Wettig, E. Speiser, S. Chandola and N. Esser, *Materials*, 2021, **14**, 4104.

44 P. Wetzel, S. Saintenoy, C. Pirri, D. Bolmont, G. Gewinner, T. P. Roge, F. Palmino, C. Savall and J. C. Labrune, *Surface Science*, 1996, **355**, 13–20.

45 A. M. Tokmachev, D. V. Averyanov, O. E. Parfenov, A. N. Taldenkov, I. A. Karateev, I. S. Sokolov, O. A. Kondratev and

V. G. Storchak, *Nature Communications*, 2018, **9**, 1672.
46 P. V. C. Medeiros, S. Stafström and J. Björk, *Phys. Rev. B*, 2014, **89**, 041407.
47 P. V. C. Medeiros, S. S. Tsirkin, S. Stafström and J. Björk, *Phys. Rev. B*, 2015, **91**, 041116.
48 G. Bihlmayer, P. Noel, D. V. Vyalikh, E. V. Chulkov and A. Manchon, *Nature Reviews Physics*, 2022, **4**, 642–659.
49 S. I. Pekar and E. I. Rashba, *Sov. Phys. JETP*, 1965, **20**, 1295–1298.
50 S. Hayami, Y. Yanagi and H. Kusunose, *Journal of the Physical Society of Japan*, 2019, **88**, 123702.
51 L. D. Yuan, Z. Wang, J. W. Luo and A. Zunger, *Physical Review Materials*, 2021, **5**, 14409.
52 L. V. Bondarenko, A. Y. Tupchaya, Y. E. Vekovshinin, D. V. Gruznev, A. N. Mihalyuk, D. A. Olyanich, Y. P. Ivanov, A. V. Matetskiy, A. V. Zotov and A. A. Saranin, *ACS Nano*, 2021, **15**, 19357–19363.